Stratocumulus-cumulus transition explained by bulk boundary layer theory

Clare E. Singer[a] and Tapio Schneider[a]

[a] *California Institute of Technology, Pasadena, California*

Corresponding author: Clare E. Singer, csinger@caltech.edu

ABSTRACT: Stratocumulus clouds occurring over eastern subtropical ocean basins dominate climatological cloudiness at low latitudes and are important for Earth's global radiative energy budget. Further west, there is an observed transition to scattered cumulus cloud cover, the so-called stratocumulus-cumulus transition (SCT), which is controlled by changing large-scale meteorological conditions. To explore the mechanisms driving the SCT, we present an extension of the traditional bulk boundary layer model (bulk model) for stratocumulus-topped boundary layers that explicitly considers cloud decoupling from the surface and subsequent cloud fraction reduction. By forcing our bulk model with boundary conditions from ERA5 reanalysis, we are able to quantitatively capture the climatological SCT. We compare the modeled SCT to satellite observations across transects of the eastern Pacific and show good agreement. The bulk model highlights the importance of surface temperature variations across the transect for controlling the SCT. We also use the bulk model to explore the sensitivity of low clouds to changing meteorological factors and show how this sensitivity is nonlinear and depends on cloud regime.

SIGNIFICANCE STATEMENT: The purpose of this study, and the companion paper Singer and Schneider (2023), is to develop a simple model to explain mechanisms controlling stratocumulus-cumulus transitions. In this first work, we describe the bulk model in cases with prescribed boundary conditions. We validate its relevance by showing how its predictions of stratocumulus-cumulus transitions across the subtropical eastern Pacific ocean basin compares to observations from satellites. We use the simple model to explore how boundary layer clouds are sensitive to different large-scale environmental factors and show how this sensitivity is nonlinear, depending on cloud regime.

1. Introduction

Stratocumulus clouds cover about 20% of tropical oceans in the annual-mean (Wood 2012; Cesana et al. 2019). They are only a few hundred meters thick, yet because of their large areal coverage, are an important regulator of Earth's radiative energy balance: by scattering sunlight, stratocumulus cool Earth by about 8 K in the global mean (Randall et al. 1984; Schneider et al. 2019). Stratocumulus cloud decks are especially common over eastern subtropical ocean basins, off the west coasts of continents, for example, near California, Peru, and Namibia, where sea surface temperatures (SSTs) are low, subsidence is strong, and there exists a strong temperature inversion at the top of the boundary layer (Klein et al. 1993; Zhang et al. 2009; Eastman et al. 2011; Chung and Teixeira 2012; Myers and Norris 2013; Bretherton and Blossey 2014).

Uniquely among clouds, stratocumulus clouds are sustained by an upside-down convective circulation that is driven by cloud-top longwave radiative cooling rather than surface heating. The longwave cooling arises because stratocumulus clouds, despite their geometric thinness, are relatively opaque to longwave radiation (Lilly 1968; Bretherton and Wyant 1997; Stevens 2006; Bellon and Geoffroy 2016; Schneider et al. 2019). Radiative cooling at the cloud tops drives the turbulent convective circulations, which are also associated with turbulent entrainment of free-tropospheric warm and dry air across the cloud top. Stratocumulus clouds exist in a delicate balance between radiative cooling at the cloud tops and warming by turbulent entrainment, on the one hand, and evaporative moistening from the surface and drying by cloud-top entrainment, on the other hand. Additionally, subsidence above the clouds works against the deepening of the cloud

layer that otherwise results from entrainment of free-tropospheric air into the cloudy boundary layer.

Meteorological factors on which cloud cover depends, commonly termed "cloud controlling factors" (CCFs) (Stevens and Brenguier 2009; Siebesma et al. 2009; Bretherton 2015), include SST, subsidence strength, the strength of the temperature inversion above the clouds (measured by either lower-tropospheric stability, LTS, or estimated inversion strength, EIS), horizontal temperature or moisture advection, wind speed, and more. A more appropriate term may be "cloud correlated factors" because the causality—whether the meteorological properties determine the clouds, or vice versa—is not always definitive. CCFs have been the focus of many previous studies (e.g., Klein et al. 1993; Stevens and Brenguier 2009; Qu et al. 2014; Klein et al. 2017).

An important test of CCFs has been the observed stratocumulus-cumulus transition (SCT). SCT describes the observed phenomenon of stratocumulus clouds dominating subtropical cloud cover just off the west coasts of continents, and the cloud cover transitioning to a state that is dominated by scattered cumulus clouds farther west, over higher SSTs and under weaker subsidence. The accepted explanation is that as the subsidence weakens, the boundary layer deepens to the point where it becomes no longer well-mixed and the clouds decouple from their surface moisture source (Bretherton and Wyant 1997). The SCT has been studied using theory (Wyant et al. 1997), high-resolution models (de Roode et al. 2016; McGibbon and Bretherton 2017; Yamaguchi et al. 2017; Neggers et al. 2017), satellite observations (Sandu et al. 2010; Chung and Teixeira 2012), and numerous field campaigns, such as ASTEX (Albrecht et al. 1995), GPCI (Teixeira et al. 2011), MAGIC (Kalmus et al. 2014), and CSET (Bretherton et al. 2019). However, it remains unclear to what extent correlations between cloud cover and CCFs in the present climate, for example, across the SCT, are informative about the climate response of clouds. For example, while a strengthened inversion in the present climate is associated with increased cloud cover (Klein et al. 1993), the relation may be reversed when considering the response to global warming (Lauer et al. 2010).

In this paper, we present a new bulk boundary layer model (bulk model) for a stratocumulus-topped boundary layer. Building from standard bulk models for the atmospheric boundary layer, we add a prognostic equation for cloud fraction, which allows the model to make quantitative predictions of the state of the cloudy boundary layer after the point of decoupling, when the cloud

fraction is less than 100%. The model is validated against observations in this paper, and against high-resolution large-eddy simulations (LES) in a companion paper (Singer and Schneider 2023).

The paper is organized as follows: Section 2 describes the bulk model. Section 3 introduces the data sources used as boundary conditions for the model and against which the results are compared. Section 4a explores sensitivities of the bulk model to idealized perturbations of boundary conditions. Section 4b compares results from the bulk model forced with reanalysis data to satellite observations of shallow clouds in the eastern Pacific. Section 5 has discussion of the assumptions in the model and key limitations. Section 6 summarizes the conclusions.

2. Bulk boundary layer model description

The general class of bulk boundary layer models describe the planetary boundary layer in terms of "bulk" or vertically-averaged quantities (Stevens 2006). The boundary layer extends up to a level, coincident with a temperature inversion and the cloud top in stratocumulus regions, whose altitude we denote as z_i (Figure 1). After vertical integration, the continuity equation simplifies to an equation for this boundary layer depth, where z_i increases due to entrainment mixing and decreases from subsidence suppression.

We formulate the bulk model in terms of liquid water static energy $s = c_p T + gz - L_v q_\ell$ and total water specific humidity $q_t = q_v + q_\ell$. These two thermodynamic quantities (referred to with generality as ψ) are (approximately) conserved under adiabatic motions of a moist air parcel. Their temporal evolution is governed by budget equations that describe a balance between diabatic source terms (ΔF_ψ) and turbulent fluxes at the surface and across the inversion. The prognostic equations for the thermodynamic variables are derived by integrating from the surface to the top of the inversion layer $z = z_i$ to give the bulk value $\hat{\psi}$. They have the form

$$z_i \frac{d\hat{\psi}}{dt} = V\Delta_{0,\psi} + w_e \Delta_{+,\psi} - \Delta F_\psi, \tag{1}$$

where the Δ_i terms represent discontinuous jumps in the quantity ψ at the surface (0) and at the inversion (+). The exchange velocity at the surface V is the product of surface wind speed (U) and an effective drag coefficient (C_d), which we will assume is the same for all thermodynamic quantities. Across the inversion, the exchange velocity is given by the entrainment velocity w_e, the form of which must be assumed and is discussed in Section 2b. To specify the surface and

cross-inversion fluxes, a vertical structure of the boundary layer must be assumed so that the bulk quantity $\hat{\psi}$ can be related to the values just above the surface $\psi(z=+\epsilon)$ and just below the inversion $\psi(z=z_i-\epsilon)$. The most common path forward is to make a well-mixed assumption where $\psi(z)=\hat{\psi}$, which simplifies the equation to

$$z_i \frac{d\psi}{dt} = V(\psi_0 - \psi) + w_e(\psi_+ - \psi) - \Delta F_\psi . \tag{2}$$

where ψ without a subscript denotes the vertically-uniform value and the subscripts 0 and + denote the value at the surface and just above the inversion, respectively.

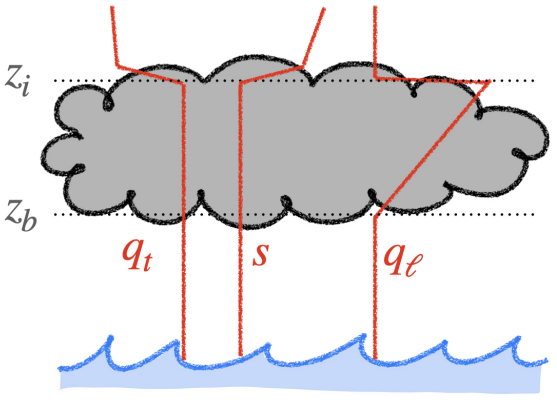

FIG. 1. Schematic of stratocumulus-topped boundary layer with representative profiles of thermodynamic quantities shown. To determine $q_\ell(z)$ from the bulk model, a mixed-layer assumption is made, where the thermodynamic quantities s and q_t are assumed to be constant with height, as illustrated.

For the liquid static energy, there is a source term from radiation, namely the radiative cooling ΔR coming from the cloud-top emitting upward longwave radiation. For moisture, we choose to neglect the sink term that would come from precipitation. Under many conditions, stratocumulus clouds have no precipitation or only very light drizzle, which justifies this assumption. In terms of the thermodynamics, however, a precipitation sink would be easy to include in future work.

The bulk model predicts the boundary layer depth and bulk energy and moisture variables given prescribed surface and above-cloud boundary conditions. These are often given as: above-cloud horizontal divergence D (or subsidence velocity), above-cloud temperature and relative humidity, which are used to calculate $s_+ = c_p T_+ + g z_i$ and $q_{t,+} = \mathrm{RH}_+ q_{\mathrm{sat}}(T_+, z_i)$, cloud-top radiative cooling

ΔR, and SST and near-surface relative humidity (RH_0), which are used to calculate $s_0 = c_p \mathrm{SST}$ and $q_{t,0} = \mathrm{RH}_0 q_{\mathrm{sat}}(\mathrm{SST}, z = 0)$.

We extend this model to include a prognostic cloud fraction (CF). Cloud fraction is relaxed toward a diagnosed state, CF′, which depends on the state of decoupling in the boundary layer and is explained in the following section.

In this form, with prescribed boundary conditions, our bulk model consists of a system of four coupled ordinary differential equations:

$$\frac{dz_i}{dt} = w_e - D z_i + w_{\mathrm{vent}} \tag{3a}$$

$$\frac{ds}{dt} = \frac{1}{z_i}\left[V(s_0 - s) + w_e(s_+ - s) - \Delta R\right] + s_{\mathrm{exp}} \tag{3b}$$

$$\frac{dq_t}{dt} = \frac{1}{z_i}\left[V(q_{t,0} - q_t) + w_e(q_{t,+} - q_t)\right] + q_{t,\mathrm{exp}} \tag{3c}$$

$$\frac{d\mathrm{CF}}{dt} = \frac{\mathrm{CF}' - \mathrm{CF}}{\tau_{\mathrm{CF}}}. \tag{3d}$$

In Eq. (3a), D is assumed constant, so $-Dz_i$ is the subsidence velocity at the cloud-top, and w_{vent} is an additional additive entrainment term used to parameterize ventilation and mixing from overshooting cumulus convective thermals. Equations (3b) and (3c) are the prognostic equations for liquid water static energy and specific humidity following from (2). In (3b), the diabatic sink term is written as ΔR, which is the cloud-top radiative cooling per unit density (units of W m kg^{-1}). In (3c), no source term appears because precipitation is neglected. In (3b) and (3c), the export terms (subscript exp) are there to represent the effect of large-scale dynamics (synoptic eddies and Hadley circulation) transporting energy and moisture laterally out of the model domain into other regions. We use the same specification as in Schneider et al. (2019) with $s_{\mathrm{exp}} = c_p(-1.2)$ J kg^{-1} day^{-1} and $q_{t,\mathrm{exp}} = \left(-6 \times 10^{-4}\right)\left(q_{\mathrm{sat}}(\mathrm{SST})/q_{\mathrm{sat}}(290\ \mathrm{K})\right)$ day^{-1}.

a. Predicted cloud fraction

Cloud fraction is relaxed to a diagnosed state CF′, which depends on the degree of decoupling of the boundary layer. When topped with stratocumulus clouds, we take the boundary layer to remain well-mixed and coupled to the ocean surface by an overturning circulation that is driven by cloud-top longwave radiative cooling. In contrast to other cloud regimes, where clouds are

formed from buoyant thermals driven by surface heating, the circulation in stratocumulus clouds is upside-down (Randall 1980). In order for the radiative cooling to keep the boundary layer well-mixed, the buoyancy anomalies created must be large enough for parcels to travel through the stably stratified cloud layer. The subcloud layer is neutrally stratified, but the cloud layer, due to latent heat release during condensation, acts as a barrier to parcels from above as they sink toward the surface. In the event where the stratification is too large compared to the radiative cooling, parcels sinking from the cloud-top will not reach the surface, and the cloud effectively becomes disconnected from its moisture supply at the ocean surface. This behavior is termed "decoupling" (Bretherton and Wyant 1997). We can diagnose boundary layer decoupling by considering the competition between cloud-top radiative cooling and surface latent heat fluxes. We introduce the decoupling parameter $\mathscr{D}$ from Bretherton and Wyant (1997),

$$\mathscr{D} = \left(\frac{\mathrm{LHF}}{\rho \Delta R}\right)\left(\frac{z_i - z_b}{z_i}\right). \tag{4}$$

When $\mathscr{D} < 1$, the boundary layer remains coupled; when $\mathscr{D} > 1$, the boundary layer is decoupled.

We parameterize the cloud fraction, based on ideas from Chung and Teixeira (2012) and observations of monthly mean climatological cloudiness, as a logistic function with a maximum of $\mathrm{CF}_{\max} = 80\%$ cloud cover and minimum of $\mathrm{CF}_{\min} = 10\%$,

$$\mathrm{CF}' = \mathrm{CF}_{\max} - \frac{\mathrm{CF}_{\max} - \mathrm{CF}_{\min}}{1 + \frac{1}{9}\exp(-m(\mathscr{D} - \mathscr{D}_c))}, \tag{5}$$

with cloud fraction smoothly varying on the nondimensional scale m. The cloud fraction is 90% depleted when the critical decoupling threshold $\mathscr{D}_c = 1$ is reached. The scale m determines the strength of the nonlinearity, but results are not strongly sensitive to m. We choose $m = 8$, which agrees well with monthly-mean observations of cloud cover (Figure 2).

The prognostic equation for cloud fraction, Eq. (3d), is a linear relaxation of the state $\mathrm{CF}(\mathscr{D})$, on a timescale $\tau_{\mathrm{CF}} = 2$ days. The timescale for the relaxation here is arbitrary, since this model is used only to predict steady-state solutions; timescales are discussed further in Section 4.

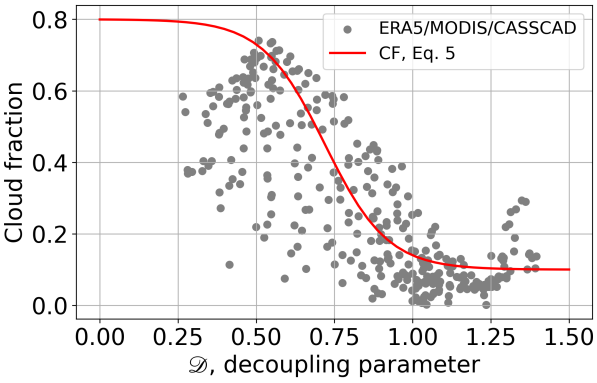

FIG. 2. Scatter plot of observations of monthly-mean cloud fraction from CASCCAD (Cesana et al. 2019) against decoupling parameter $\mathscr{D}$. LHF is taken from ERA5 reanalysis, and observations of cloud-top radiative cooling from Zheng et al. (2021). We assumed a fixed $(z_i - z_b)/z_i = 0.4$. The red line shows the analytical form of cloud fraction predicted from Eq. 5 with $m = 8$.

One aspect that is neglected here, due to our previous assumption not to include precipitation in the moisture budget, is that we do not consider the possibility of drizzle-induced stratocumulus breakup (Yamaguchi et al. 2017; Uchida et al. 2010; Stevens et al. 2005; Geoffroy et al. 2008; Prabhakaran et al.). Precipitation can deplete the cloud layer of moisture through a different mechanism than the cloud-top cooling route captured by decoupling parameter, and lead to cloud fraction reduction while $\mathscr{D} < 1$. This could be explored in future work.

b. Entrainment closure

To close the system of equations, we must specify the entrainment velocity. We parameterize it here such that entrainment mixing balances radiative cooling in the steady state: an "energy-balance entrainment" closure (Bretherton and Wyant 1997). The entrainment velocity is proportional to the radiative cooling and inversely proportional to the buoyancy jump across the inversion

$$w_e = \frac{\Delta R}{s_{v+} - s_v}. \tag{6}$$

We write this with the virtual liquid static energy $s_v = c_p T_v + gz - L_v q_\ell$ which accounts for the buoyancy effects of water vapor through the virtual temperature $T_v = (R_m/R_d)T$.

An additional additive entrainment term, w_{vent}, is introduced which depends on the cloud fraction. The physical idea is that in a cumulus state, buoyant plumes will overshoot z_i and lead to additional entrainment or ventilation and growth of the boundary layer. This is modeled as

$$w_{\text{vent}} = \alpha_{\text{vent}} \left(\frac{\text{CF}_{\text{max}} - \text{CF}}{\text{CF}_{\text{max}} - \text{CF}_{\text{min}}} \right) \tag{7}$$

where $\alpha_{\text{vent}} = 1.69$ mm s^{-1}. This parameter value was selected as described in Singer and Schneider (2023) to best fit the LES results from Schneider et al. (2019).

c. Cloud-top cooling closure

Rather than specifying the cloud-top cooling directly as an independent boundary condition, we parameterize the radiative cooling as a function of the longwave absorbers in the free-troposphere above the cloud (CO_2 and H_2O). Conceptually, higher concentrations of absorbers will decrease the cloud-top cooling because the atmosphere will be optically thicker in the infrared, and the downwelling longwave radiation hitting the cloud-top will be coming from closer levels, or higher temperatures, reducing the net upward longwave flux. Mathematically, we can write the cloud-top radiative cooling term as the difference between the upwelling radiation emitted from the cloud top and the downwelling radiation emitted back from the atmosphere. The upwelling radiation is emitted at the cloud top temperature T_{ct}, while the downwelling radiation comes from a temperature $T_{ct} - \Delta T_e$. The cloud-top radiative cooling then is

$$\Delta R = \text{CF} \cdot \epsilon_c \sigma \left(T_{ct}^4 - (T_{ct} - \Delta T_e)^4 \right), \tag{8}$$

where $\epsilon_c = 0.9$ is the cloud emissivity. The cloud emissivity is assumed constant, which is reasonable given large enough liquid water paths as the longwave emission tends to saturate around 20 g m^{-2} (Petters et al. 2012). We then parameterize ΔT_e, which depends on the optical thickness of the atmosphere above the cloud top, or the concentrations of CO_2 and H_2O as,

$$\Delta T_e = a_0 + a_1 \ln(\text{CO}_2) + a_2 \ln(q_{t,+}). \tag{9}$$

We fit the parameters $a_0 = -10.1$ K, $a_1 = 3.1$ K, and $a_2 = 5.3$ K based on the radiative transfer model (RRTMG) in the LES simulations presented in Schneider et al. (2019) (see Fig. 3).

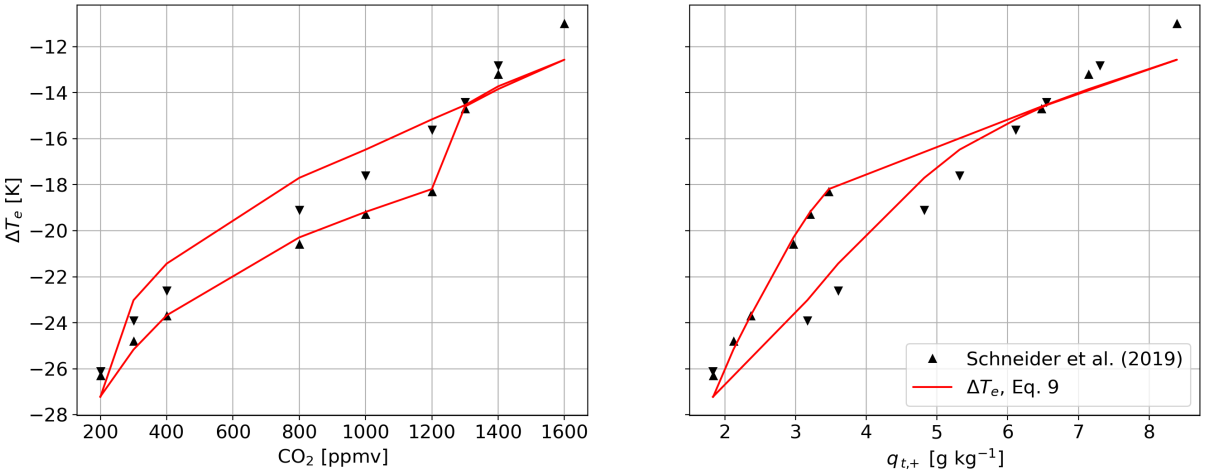

FIG. 3. Difference between cloud-top temperature and effective downwelling emission temperature (ΔT_e) fit to LES from Schneider et al. (2019). Shown with ΔT_e plotted against (a) the CO_2 concentration and (b) the above-cloud specific humidity $q_{t,+}$. Upward (downward) pointing triangle markers are LES experiments with increasing (decreasing) CO_2.

Purely for diagnostic purposes, we introduce a well-mixed assumption, with $s(z)$ and $q_t(z)$ constant within the boundary layer, to diagnose the liquid water in the cloud layer (as shown in Figure 1). The liquid water specific humidity is diagnosed as the excess above saturation,

$$q_\ell(z) = q_t - \frac{R_d}{R_v}\left(\frac{p_{\rm sat}(T(z))}{p(z) - p_{\rm sat}(T(z))}\right),$$

with the saturation vapor pressure (Romps 2008)

$$p_{\rm sat}(z) = e_0 \exp\left(-\frac{L_0}{R_v}\left(\frac{1}{T(z)} - \frac{1}{T_0}\right)\right).$$

3. Observational data for comparison and model validation

We use monthly observations of low-cloud cover (CF) from the CASCCAD dataset, which is a combined product using Cloudsat and CALIPSO (Cesana et al. 2019). The CASSCAD algorithm separates observed clouds by cloud type, but here we use the total "low" cloud cover product. The

CASSCAD product has monthly mean cloud fraction observations from January 2007 to December 2016.

The monthly climatological observations of cloud-top radiative fluxes come from Zheng et al. (2019, 2021). This is a combined product using observations from MODIS, NCEP reanalysis, and the Santa Barbara DISORT Atmospheric RTM.

All other "observations" are from ERA5 reanalysis (Hersbach et al. 2020); we use the same 10-year period of the CASSCAD observations. To obtain the fields used as boundary conditions to the bulk model (shown in Figure 4), the following daily ERA5 fields are used: sea surface temperature (SST), 10-m horizontal winds, vertical velocity at 500 hPa, relative humidity at 500 hPa (RH_{500}), surface pressure, 2-m temperature, temperature at 700 hPa, and temperature at 850 hPa. Estimated inversion strength (EIS) is calculated according to Wood and Bretherton (2006) (their Eq. 4). Divergence at 500 hPa (D_{500}) is calculated from vertical velocity as in Tan et al. (2016), with an assumed quadratic profile in pressure. Surface wind speed U is calculated from 10-m horizontal velocity components as $U = \sqrt{||u||^2 + ||v||^2}$.

We use daily reanalysis data for NH summer (JJA). Observations are filtered to only include days with mean subsidence across the North East Pacific (NEP) transect because the bulk model can only be applied to regions of subsidence. The results are insensitive to exactly how this filtering is done. Appendix 6 discusses this in more detail.

The monthly mean fields of SST, U, EIS, D_{500}, RH_{500}, and CF are shown in Figure 4. These fields, the canonical CCFs, are the boundary conditions given as input to the bulk model, along with the resulting cloud fraction, which is the output of the model. The red dotted line shows the transect from the coast of California to near Hawaii analyzed throughout this study. Below each map in Figure 4, the subplots show the climatological mean values of the CCFs along this transect in summer (JJA) as well as their year-to-year standard deviations (shading).

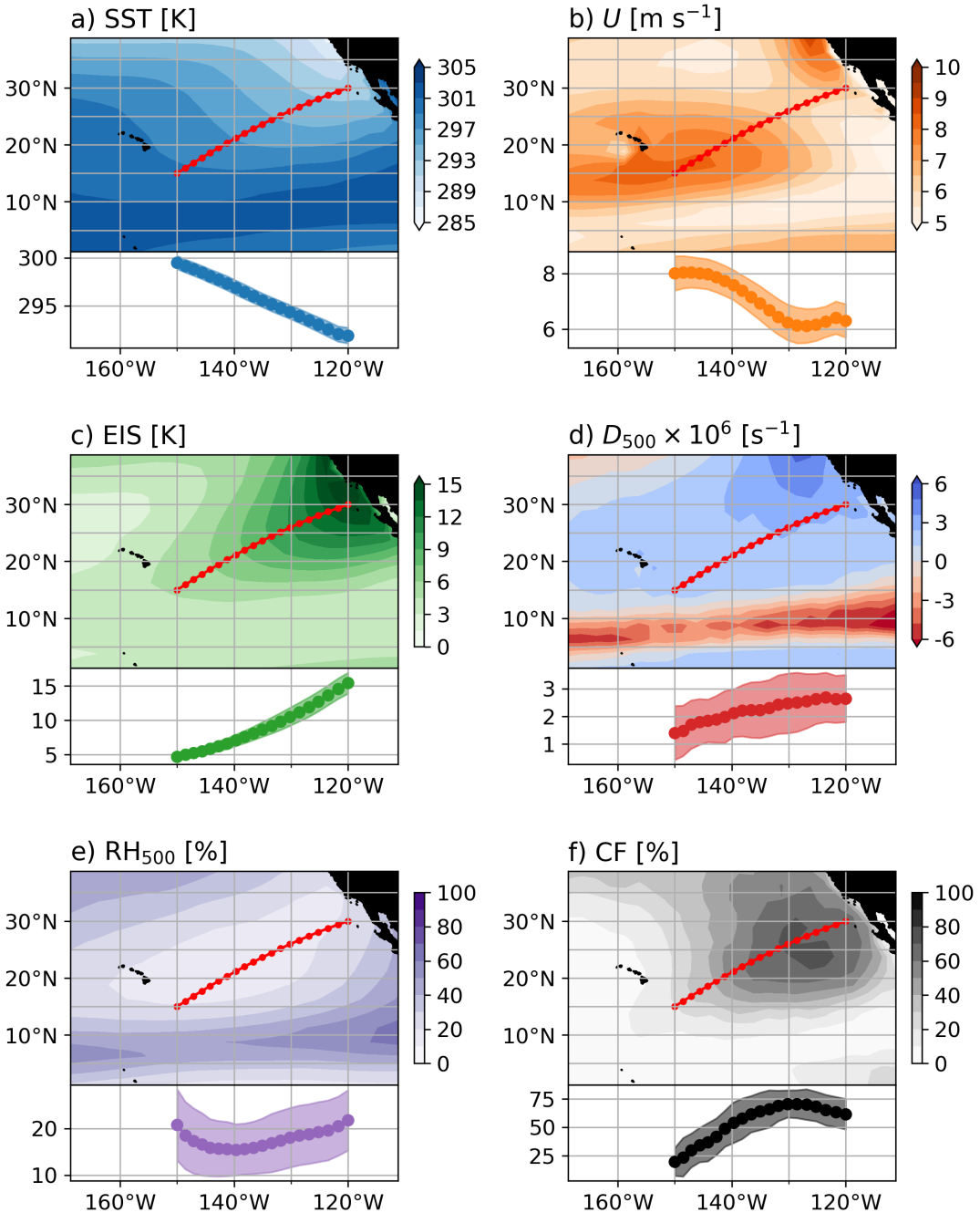

231 FIG. 4. Boundary conditions from reanalysis in JJA for the North East Pacific (NEP) SCT region. Shown
232 are: (a) SST, (b) surface wind speed, (c) estimated inversion strength, (d) large-scale horizontal divergence, (e)
233 above-cloud relative humidity, and (f) cloud fraction. The transect is shown in the red line. Mean and standard
234 deviations from the JJA climatology (2007-2016) are plotted in the insets below each map.

4. Results

The bulk model predicts the evolution of the cloudy boundary layer in addition to the steady-state result. The timescale for convergence to the steady-state is set by the slowest timescale in the problem. The thermodynamic variables ψ evolve on a timescale $\tau_\psi = z_i/(V + w_e)$, and the boundary layer depth evolves on a timescale $\tau_{z_i} = D^{-1}$ (Bretherton et al. 2010; Jones et al. 2014). Numerically, these timescales are on the order $\tau_\psi = 20$ hours and $\tau_{z_i} = 46$ hours. We introduce here a fourth equation for cloud fraction with a specified timescale $\tau_{\mathrm{CF}} = 2$ days, which is longer than these others, such that cloud fraction responds to changes in the boundary layer properties, without introducing large positive feedbacks that lead to oscillations in the system. Because the cloud fraction timescale is somewhat arbitrary, and because all timescales are longer than a diurnal cycle, yet we do not include variable diurnal forcing, the model is only used to examine steady-state results and does not give realistic information about the temporal evolution of the boundary layer. Furthermore, we neglect synoptic-scale variability, as well as realistic Lagrangian trajectories that would change boundary conditions on the order of days. The steady-state behavior gives useful insight into mechanisms controlling climatological cloudiness, but it does not provide realistic predictions of individual trajectories.

a. Idealized linear response to perturbations

The bulk model solution is dependent on all boundary conditions, or CCFs, though to some more strongly than to others. Figure 5 shows the steady-state results of cloud fraction and in-cloud LWP predicted by the bulk model for a variety of conditions. Each subplot shows perturbations of just one boundary condition while the rest remain fixed; included are the five meteorological boundary conditions from Figure 4 and CO_2. Perturbations are applied to two idealized states: a high-cloud fraction stratocumulus (Sc) state (solid lines), and a low-cloud fraction cumulus (Cu) state (dotted lines). SST (290 vs. 295 K) and IS (12 vs. 6 K) are used to distinguish between these two regimes.

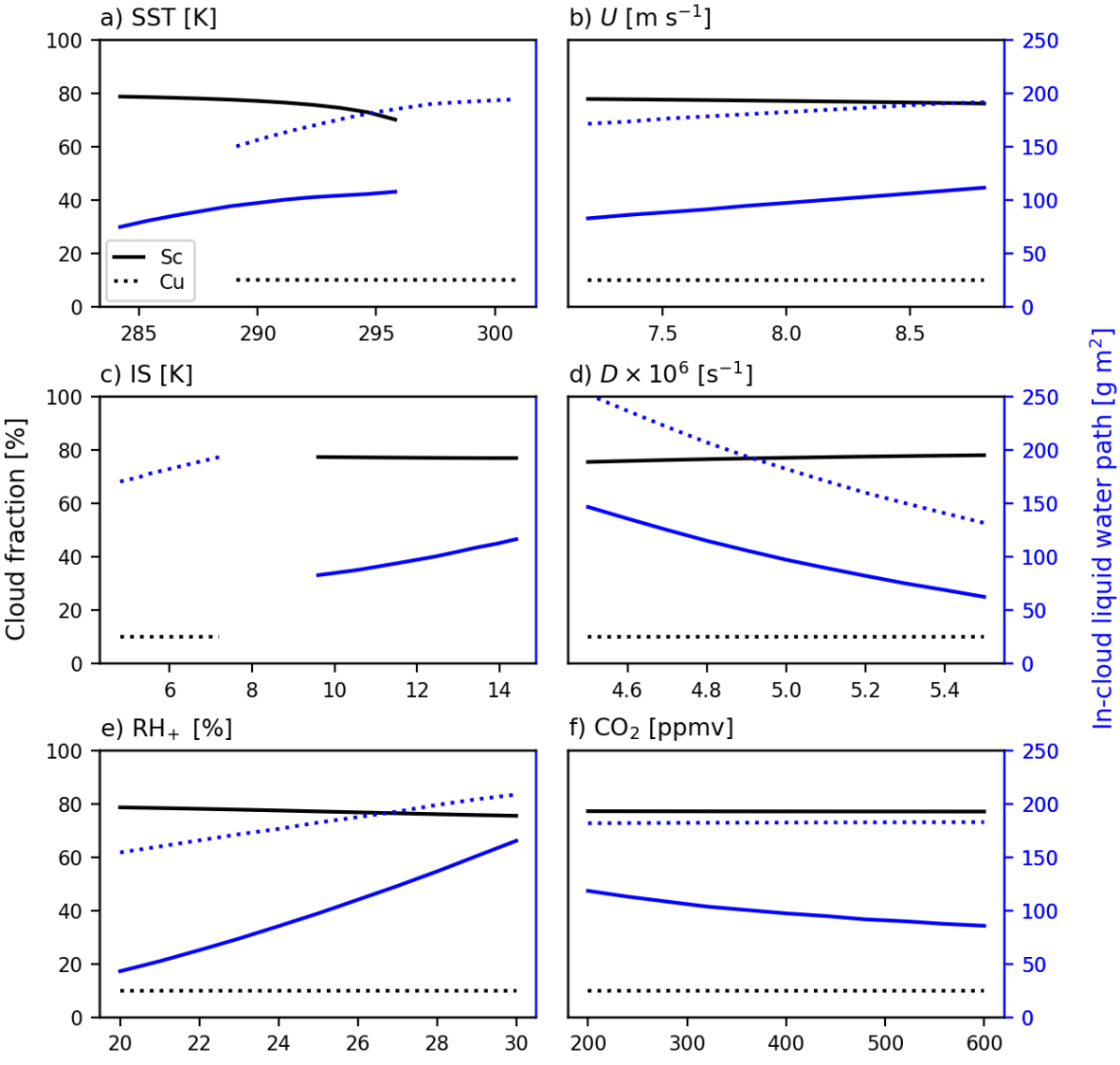

FIG. 5. CF and in-cloud LWP when varying individual boundary condition parameters around some reference values typical of stratocumulus conditions (solid lines) and cumulus state (dotted lines). Boundary conditions varied are: (a) SST, (b) surface wind speed U, (c) inversion strength (IS, the actual inversion prescribed in the bulk model), (d) large-scale horizontal divergence D, (e) above-cloud relative humidity RH$_+$, and (f) CO_2.

For perturbations about the stratocumulus state (solid lines), cloud fraction is relatively fixed at the maximum value (80%), except at the warmest SSTs when cloud fraction starts to drop off (Fig. 5a). The response of in-cloud liquid water path (LWP) is positive for SST, wind speed, above-cloud humidity, and inversion strength and negative for subsidence and CO_2. While the boundary

layer remains in the coupled state, higher SSTs and stronger winds lead to greater LHFs which increase cloud moisture; a more humid free-troposphere and stronger inversion reduce entrainment drying and increase LWP. On the other hand, stronger subsidence shoals the boundary layer and reduces cloud thickness and LWP, and increased CO_2 decreases cloud-top cooling and reduces LWP. However, higher SSTs and hence stronger LHFs also increase decoupling and ultimately lead to reduced CF, which is seen in Fig. 5a; hence increasing SST has opposite sign effects on CF and LWP.

For perturbations about the cumulus state (dotted lines), cloud fraction is pinned to its minimum value (10%). The sign of the in-cloud LWP response to each CCF is the same, though the magnitude varies compared to the perturbations around the stratocumulus state. Most notable are the nonlinear responses to above-cloud humidity (Fig. 5d) and CO_2 (Fig. 5f). The LWP response from the Cu state is weaker than from the Sc state, and the response to CO_2 is nearly nonexistent here. The sensitivity of Cu to subsidence is slightly stronger compared to Sc (Fig. 5c).

b. Stratocumulus-cumulus transition across North East Pacific

To validate the bulk model, we predict the cloud fraction given the observed large-scale conditions and compare it to the observed cloud fraction across the NEP SCT transect. The result is shown in Figure 6a. We predict the cloud cover in two ways: 1) by forcing the bulk model to steady-state with the climatological mean boundary conditions over the observed 10-year period (pink dashed line), and 2) by forcing the bulk model to steady-state with 100 randomly chosen days from the same period (pink solid line). Because the cloudiness of the boundary layer is a nonlinear process, and the bulk model exhibits strongly nonlinear behavior, the cloud fraction predicted from the monthly mean boundary conditions is different from the mean of the cloud fraction predicted from daily conditions.

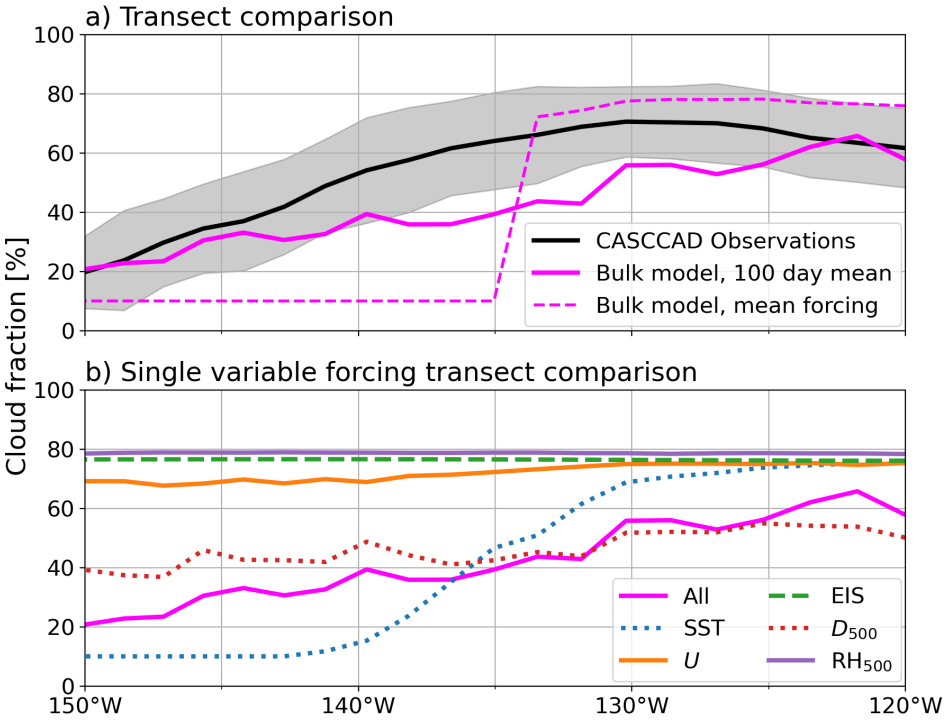

FIG. 6. Cloud fraction along North East Pacific (NEP) stratocumulus-cumulus transect. (a) Mean JJA climatology (2007-2016) and standard deviation from CASCCAD observations (black), mean of bulk model forced by ERA5 boundary conditions from 100 randomly chosen days from the subsidence-only reanalysis record over the same time period (pink, solid), and bulk model prediction forced by climatological boundary conditions (pink, dashed). (b) Cloud fraction predicted by bulk model with single-variable forcing, again averaged over 100 randomly chosen days: SST (blue), U (orange), EIS (green), D (red), and RH_+ (purple); all variable forcing duplicated for comparison (pink). Only variations in SSTs alone produce a transition along the transect, through other factors also contribute to the total.

The nonlinearity in the bulk model from the strong positive feedback between cloud cover and cloud-top radiative cooling results in sharp transitions day to day. Over long-time averages, this results in a smooth curve. However, when the bulk model is forced with the mean of the reanalysis-derived boundary conditions, a sharp transition is predicted.

Further, we investigate which CCFs most strongly control the transition by varying only one at a time in the simulations (Figure 6b). We observe that SST alone is sufficient to create a SCT, but the other CCFs are not. The other factors do contribute and create variability in cloud thickness

and decoupling strength, but each in itself is insufficient to induce a full transition to a low cloud fraction, Cu-like, state.

Moving beyond our analysis of a one-dimensional transect, we compare the observed cloud fraction to the predicted cloud fraction in the entire NEP region. Figure 7 compares the observed cloud fraction to that predicted by the bulk model. The bulk model cloud fraction is the mean predicted value from the model averaged over approximately 100 randomly chosen days from the 10-year CASCCAD record. A total of 200 individual days were randomly selected, but since the bulk model was only applied in places with mean daily subsidence, the number of days included in the average varies by location (from 74 to 181).

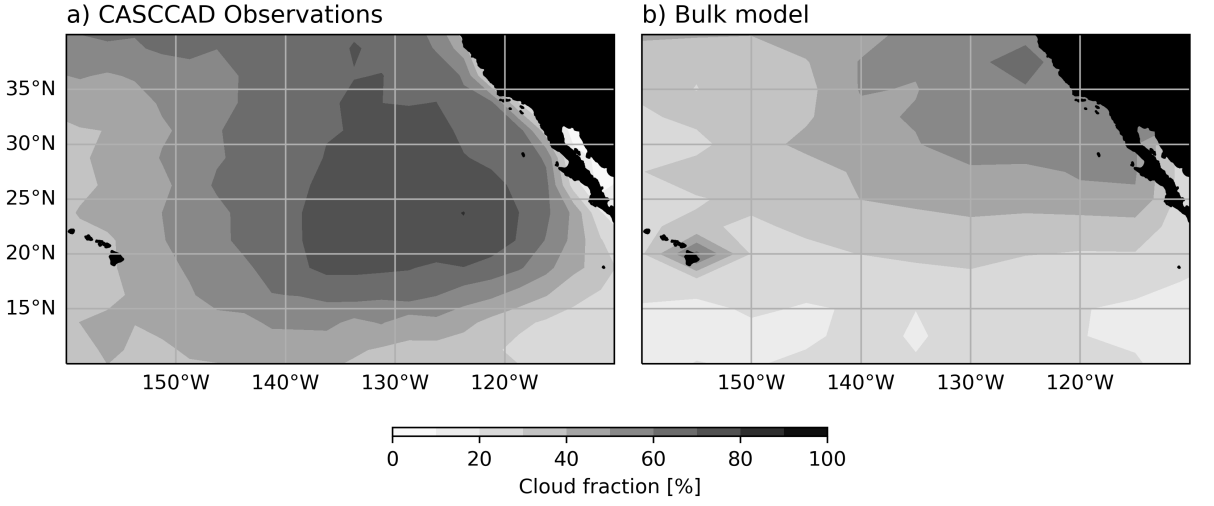

FIG. 7. (a) Observed and (b) predicted cloud fraction climatology across the North East Pacific region during JJA. Prediction from bulk model is the average over approximately 100 randomly chosen days from the 10-year period 2006-2017. For each day, the bulk model is driven with climatological boundary conditions of SST, U, EIS, D_{500}, and RH_{500} from ERA5 reanalysis and run to steady-state. The resulting cloud fraction is averaged to produce this mean climatology plot.

Extending the analysis of the response of the cloud to perturbations from idealized mean states (Figure 5), Figure 8 shows the dependence of all-sky LWP on each boundary condition for observed states across the NEP region. In the steady-state, both the cloud fraction and in-cloud LWP respond to perturbations in boundary conditions. All-sky LWP combines changes in cloud fraction and in-cloud LWP. The goal of this analysis is to illustrate how the sensitivity to changes in the various boundary conditions depends on the mean state from which we are perturbing.

Changes in LWP are shown normalized by the observed year-to-year variability for each boundary condition parameter (shown in Fig. 4), except for CO_2 where changes are shown relative to a $\sigma_{x_i} = 100$ ppmv perturbation. Specifically, the difference in steady-state LWP for a forcing of $x_i \pm \sigma_{x_i}/2$ is plotted for each factor x_i, where σ_{x_i} is the year-to-year variability during JJA in the 10-year record (2006-2017). This normalization is important to put the magnitude of perturbations of each boundary condition into context; for example, a 5 K change in SST is not easily comparable to a 10% change in above-cloud relative humidity. Because the normalization is based on the temporal variability of each boundary condition parameter, not the spatial variability, the results do not correspond directly to the sensitivities along the transect shown in Figure 6b.

In general, the results agree very well with Figure 5. The all-sky LWP is mostly reflecting in-cloud LWP changes, except at the edges of the region where transitions between cloud states may occur. We saw from the perturbation analysis before that LWP is most sensitive to changes in subsidence and above-cloud humidity (Figure 5). Stronger subsidence thins the boundary layer and reduces LWP, while a more humid free-troposphere suppresses entrainment drying and increases LWP. Sensitivity to SST, EIS, and CO_2 is quite weak, but positive for SST and EIS and negative for CO_2, agreeing with Fig. 5. The sensitivity of all-sky LWP to surface wind speeds has the most complex spatial structure. In the center of the stratocumulus region, there is almost no sensitivity to wind speed, but toward the edges, stronger wind speeds result in more LWP due to increase LHF, until the LHF becomes too large and results in decoupling, which then dramatically reduces all-sky LWP (seen by sharp transition from red to blue colors at the edges).

5. Discussion

Our bulk model is able to capture key features of the stratocumulus-cumulus transition (SCT) and highlights the key mechanisms that drive the breakup of stratocumulus clouds along these westward transects. However, the model makes many assumptions that cannot represent the full complexity of the atmospheric boundary layer. Here we present a short discussion of some key limitations and imperfections of this model, some of which may be interesting avenues of future research.

First, the model has a limited representation of the effect of decoupling on the vertical structure of the boundary layer. In the derivation in Section 2, we introduce our bulk model in the more general

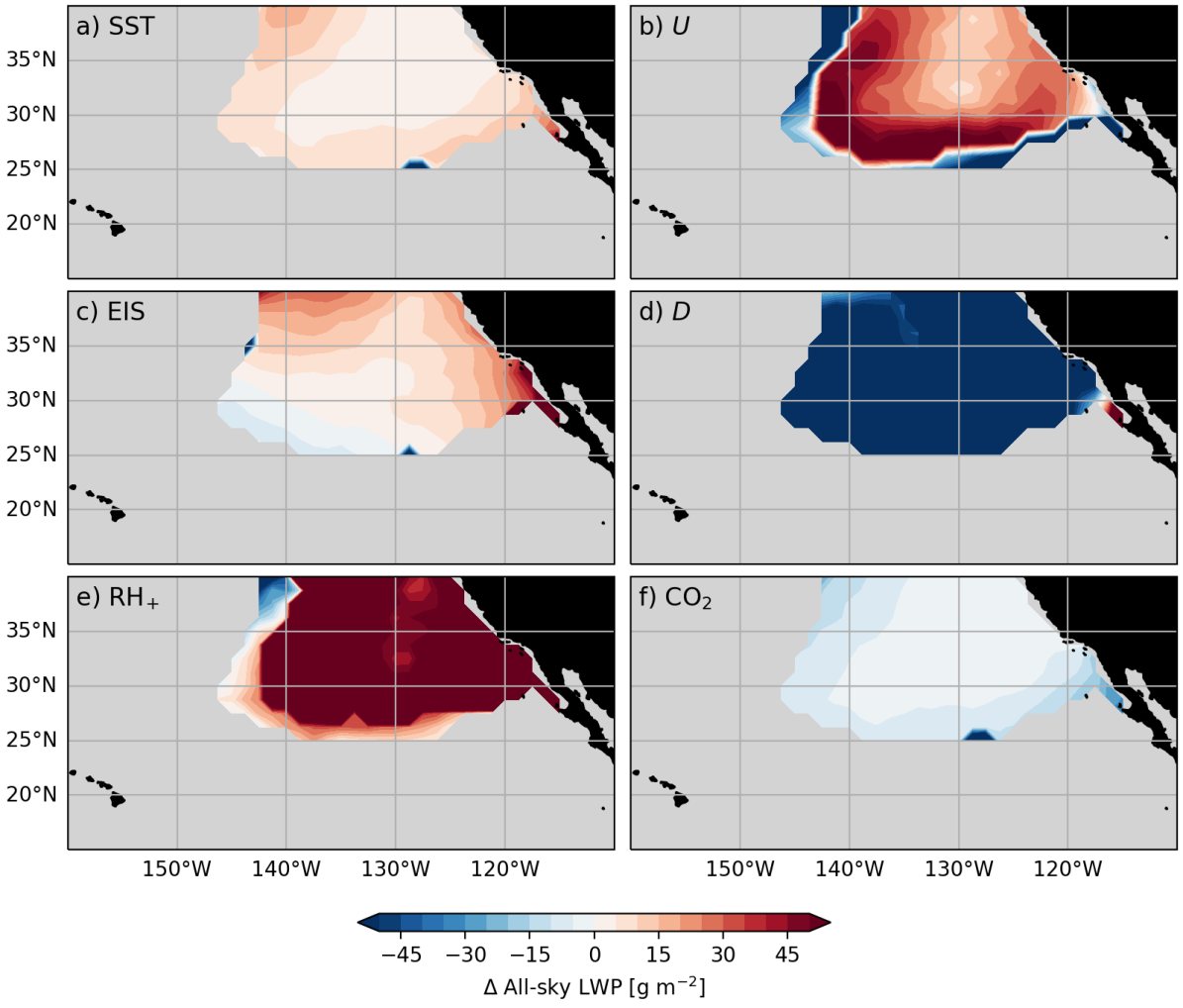

334 FIG. 8. Change in all-sky LWP given a normalized perturbation of each CCF at each location across the NEP
335 region (in JJA). Regions with mean CF < 0.5 are shaded in grey. The sensitivities to each CCF vary in space
336 depending on the initial state of the cloud, highlighting the nonlinear response. LWP increases with SST and
337 above-cloud humidity everywhere, decreases with subsidence and CO_2 everywhere, while the sign of response
338 to surface wind speed and EIS varies in space.

359 form, not as a mixed-layer model, highlighting the flexibility of this approach to include more
360 nuanced representations of the vertical structure. However, in the end we did make the well-mixed
361 assumption in how we specified the form of the surface fluxes. And we included a somewhat
362 artificial ventilation term, w_{vent}, which represents extra mixing by positively buoyant thermals
363 that overshoot the inversion. Future work could look into extending this model by including a

non-well-mixed vertical structure throughout, or only after decoupling, along the lines of what was done by Schalkwijk et al. (2013) or Salazar and Tziperman (2023).

Second, this bulk model represents a single column of the atmosphere and neglects advection, or the Lagrangian history of the air parcels, which is known to be important (Sandu et al. 2010). Previous work has found that temperature advection can be an important cloud controlling factor (e.g., Scott et al. 2020), but based on Figure 6, in the monthly-mean sense, we are able to reproduce the salient features of the observed SCT without this. Including temperature advection into the bulk model can be done trivially by including an additional source term on Equation 3b, and could be explored in future work.

Third, the bulk model assumes that cloud emissivity (in Equation 8) is independent of LWP. We explored making the emissivity dependent on LWP following Stephens (1978) as

$$\epsilon_c = 1 - e^{-\mathrm{LWP}/\mathrm{LWP}_0},$$

where $\mathrm{LWP}_0 = 7$ g m^{-2}. We chose not to use this option for this study as it proved not to be critical for the qualitative results, and it introduced an additional positive feedback in the system that made interpretations more difficult. As with most choices made while developing this model, the goal was a minimal representation of the important physics, while retaining as simple a model as possible. In this vein, the fourth major limitation is the lack of temporal variability. The bulk model is used to make steady-state predictions, and given the timescales of the problem, the system takes $O(10$ days$)$ to equilibrate. However, the model neglects the diurnal cycle, synoptic variability, and seasonal variability when solving for these equilibrium solutions. Again, this is done to retain simplicity by keeping the boundary conditions fixed, but it could be relaxed in future work if desired.

6. Conclusions

Stratocumulus clouds are a radiatively important feature of Earth's climate because they contribute to shortwave reflectance without compensating greenhouse warming. They appear in specific locations on Earth, predominantly over eastern subtropical ocean basins due to their sensitive dependence on large-scale meteorological factors (CCFs). These CCFs have been used many times previously as a basis for constraining stratocumulus response to climate change. However,

these models rely only on linear, statistical correlations between CCFs and cloudiness. In this work we presented a nonlinear and physical, but still simple, bulk boundary layer model for low cloudiness.

Our model is similar to traditional mixed-layer models for stratocumulus-topped boundary layers, but we extended it to include a prognostic equation for cloud fraction. Cloud fraction in our model depends on the strength of boundary layer coupling as diagnosed by the decoupling parameter $\mathscr{D} = (\mathrm{LHF}/\Delta R) \cdot ((z_i - z_b)/z_i)$. The decoupling idea is based on Bretherton and Wyant (1997) and Chung and Teixeira (2012). We included a simple representation of radiative transfer to explicitly link the cloud-top radiative cooling to concentrations of greenhouse gases (CO_2 and H_2O) in the overlying free-troposphere. We showed how our bulk model is sensitive to perturbations in various large-scale environmental conditions, CCFs and CO_2. We validated our bulk model by comparing predictions of cloud fraction to observations from the CALIPSO and CloudSat satellites across the North East Pacific stratocumulus-to-cumulus transition transect.

In some ways this model is overly simple, neglecting some important physical processes, and it should not be viewed as a parameterization. However, because this model is able to capture important features of the SCT, it is useful as a conceptual tool. In a companion paper, we elaborate further on the mechanisms governing SCTs in this model and use it to explore exotic climates with very high CO_2 concentration (Singer and Schneider 2023).

Acknowledgments. CES acknowledges support from NSF Graduate Research Fellowship under Grant No. DGE-1745301. This research was additionally supported by the generosity of Eric and Wendy Schmidt by recommendation of the Schmidt Futures program and by Charles Trimble. We thank Zhaoyi Shen for many helpful discussions in early stages of this project.

Data availability statement. The bulk model, along with examples reproducing all figures in this paper and documentation, is available on Github (`https://github.com/claresinger/MixedLayerModel.jl`).

APPENDIX

Subsetting daily reanalysis data

On long time scales, e.g., over monthly means, the North East Pacific (NEP) is a region of subsidence (see Fig. 4d). However, on daily timescales, there can be net upward motion in any location. The bulk model assumes there is subsidence, and from the equation of mass conservation (3a), the model will not reach steady state if D is negative. Therefore, when forcing the bulk model with boundary conditions from reanalysis observations, we only want to choose observations on days with subsidence.

There are two logical ways to subset the data to exclude observations of $D < 0$. They are both shown in Figure A1. 1) We can exclude only the locations of upward motion on certain days (black dotted). The downside to this approach is that it will result in unequal numbers of observations at different spatial locations. Or, 2) we can exclude all locations on days with any upward motion along the whole transect (red). The downside to this approach is that it more severely filters the data, and we are left with fewer total observations.

However, we can see that both of these approaches have similar mean transect profiles. The transects for all quantities except horizontal divergence (D_{500}) are similar to the unfiltered data with all days (black solid). For simplicity, to keep the number of total observations at each spatial point equal, and because we retain enough data to reconstruct the climatological picture, we choose to keep only days where there is subsidence everywhere along the transect (red).

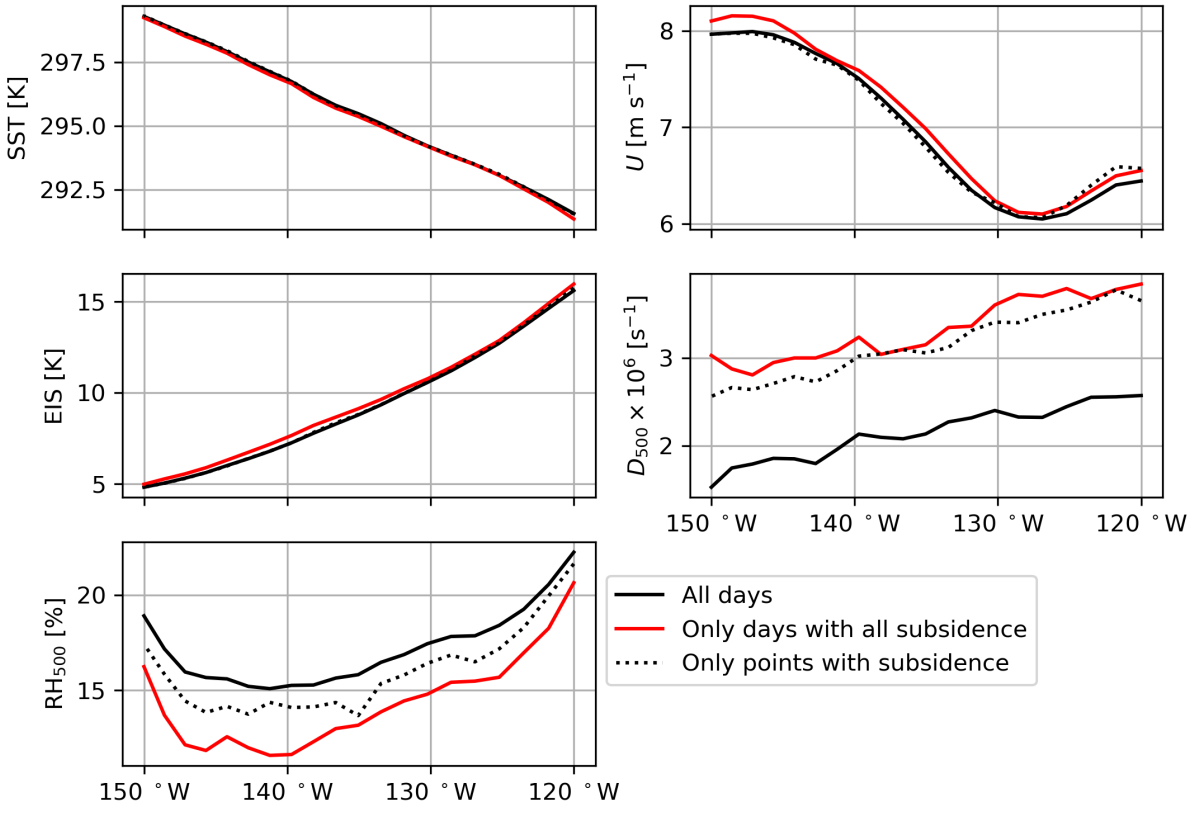

FIG. A1. NEP transect of CCFs – sea surface temperature (SST), surface wind speed (U), estimated inversion strength (EIS), 500 hPa horizontal divergence (D_{500}), and 500 hPa relative humidity (RH_{500}) – showing all days in JJA 2007–2016 (black solid), only days with subsidence along the entire transect (red solid), and only points with local subsidence (black dotted).

References

Albrecht, B. A., and Coauthors, 1995: The Atlantic stratocumulus transition experiment—ASTEX. *Bull. Amer. Meteor. Soc.*, **76 (6)**, 889–904, https://doi.org/10.1175/1520-0477(1995)076<0889:TASTE>2.0.CO;2.

Bellon, G., and O. Geoffroy, 2016: How finely do we need to represent the stratocumulus radiative effect? *Quart. J. Roy. Meteor. Soc.*, **142 (699)**, 2347–2358, https://doi.org/10.1002/qj.2828.

Bretherton, C. S., 2015: Insights into low-latitude cloud feedbacks from high-resolution models. *Philos. Trans. R. Soc. A Math. Phys. Eng. Sci.*, **373 (2054)**, https://doi.org/10.1098/rsta.2014.0415.

Bretherton, C. S., and P. N. Blossey, 2014: Low cloud reduction in a greenhouse-warmed climate: Results from Lagrangian LES of a subtropical marine cloudiness transition. *J. Adv. Model. Earth Syst.*, **6 (1)**, 91–114, https://doi.org/10.1002/2013MS000250.

Bretherton, C. S., J. Uchida, and P. N. Blossey, 2010: Slow manifolds and multiple equilibria in stratocumulus-capped boundary layers. *J. Adv. Model. Earth Syst.*, **2**, 1–20, https://doi.org/10.3894/JAMES.2010.2.14.

Bretherton, C. S., and M. C. Wyant, 1997: Moisture transport, lower-tropospheric stability, and decoupling of cloud-topped boundary layers. *J. Atmos. Sci.*, **54**, 148–167.

Bretherton, C. S., and Coauthors, 2019: Cloud, aerosol, and boundary layer structure across the northeast Pacific stratocumulus–cumulus transition as observed during CSET. *Mon. Weather Rev.*, **147 (6)**, 2083–2103, https://doi.org/10.1175/MWR-D-18-0281.1.

Cesana, G., A. D. Del Genio, and H. Chepfer, 2019: The cumulus and stratocumulus CloudSat-CALIPSO dataset (CASCCAD). *Earth Syst. Sci. Data*, **11 (4)**, 1745–1764, https://doi.org/10.5194/essd-11-1745-2019.

Chung, D., and J. Teixeira, 2012: A simple model for stratocumulus to shallow cumulus cloud transitions. *J. Climate*, **25 (7)**, 2547–2554, https://doi.org/10.1175/JCLI-D-11-00105.1.

de Roode, S. R., and Coauthors, 2016: Large-eddy simulations of EUCLIPSE–GASS Lagrangian stratocumulus-to-cumulus transitions: Mean state, turbulence, and decoupling. *J. Atmos. Sci.*, **73 (6)**, 2485–2508, https://doi.org/10.1175/JAS-D-15-0215.1.

Eastman, R., S. G. Warren, and C. J. Hahn, 2011: Variations in cloud cover and cloud types over the ocean from surface observations, 1954–2008. *J. Climate*, **24**, 5914–5934, https://doi.org/10.1175/2011JCLI3972.1.

Geoffroy, O., J.-L. Brenguier, and I. Sandu, 2008: Relationship between drizzle rate, liquid water path and droplet concentration at the scale of a stratocumulus cloud system. *Atmos. Chem. Phys.*, **8**, 4641–4654, https://doi.org/10.5194/acp-8-4641-2008.

Hersbach, H., and Coauthors, 2020: The ERA5 global reanalysis. *Quart. J. of the Roy. Meteor. Soc.*, **146 (730)**, 1999–2049, https://doi.org/https://doi.org/10.1002/qj.3803.

Jones, C. R., C. S. Bretherton, and P. N. Blossey, 2014: Fast stratocumulus time scale in mixed layer model and large eddy simulation. *J. Adv. Model. Earth Syst.*, **6 (1)**, 206–222, https://doi.org/10.1002/2013MS000289.

Kalmus, P., M. Lebsock, and J. Teixeira, 2014: Observational boundary layer energy and water budgets of the stratocumulus-to-cumulus transition. *J. Climate*, **27 (24)**, 9155–9170, https://doi.org/10.1175/JCLI-D-14-00242.1.

Klein, S. A., A. Hall, J. R. Norris, and R. Pincus, 2017: Low-cloud feedbacks from cloud-controlling factors: A review. *Surveys in Geophysics*, **38**, 1307–1329, https://doi.org/10.1007/978-3-319-77273-8_7.

Klein, S. A., D. L. Hartmann, S. A. Klein, and D. L. Hartmann, 1993: The seasonal cycle of low stratiform clouds. *J. Climate*, **6 (8)**, 1587–1606, https://doi.org/10.1175/1520-0442(1993)006<1587:TSCOLS>2.0.CO;2.

Lauer, A., K. Hamilton, Y. Wang, V. T. J. Phillips, and R. Bennartz, 2010: The impact of global warming on marine boundary layer clouds over the eastern Pacific—a regional model study. *J. Climate*, **23**, 5844–5863, https://doi.org/10.1175/2010JCLI3666.1.

Lilly, D. K., 1968: Models of cloud-topped mixed layers under a strong inversion. *Quart. J. Roy. Meteor. Soc.*, **94**, 292–309, https://doi.org/10.1002/qj.49709440106.

McGibbon, J., and C. S. Bretherton, 2017: Skill of ship-following large-eddy simulations in reproducing MAGIC observations across the northeast Pacific stratocumulus to cumulus transition region. *J. Adv. Model. Earth Syst.*, **9 (2)**, 810–831, https://doi.org/10.1002/2017MS000924.

Myers, T. A., and J. R. Norris, 2013: Observational evidence that enhanced subsidence reduces subtropical marine boundary layer cloudiness. *J. Climate*, **26 (19)**, 7507–7524, https://doi.org/10.1175/JCLI-D-12-00736.1.

Neggers, R. A. J., and Coauthors, 2017: Single-column model simulations of subtropical marine boundary-layer cloud transitions under weakening inversions. *J. Adv. Model. Earth Syst.*, **9**, 2385–2412, https://doi.org/10.1002/2017MS001064.

Petters, J. L., J. Y. Harrington, and E. E. Clothiaux, 2012: Radiative-dynamical feedbacks in low liquid water path stratiform clouds. *J. Atmos. Sci.*, **69 (5)**, 1498–1512, https://doi.org/10.1175/JAS-D-11-0169.1.

Prabhakaran, P., F. Hoffmann, and G. Feingold, ????: Evaluation of pulse aerosol forcing on marine stratocumulus clouds in the context of marine cloud brightening. https://doi.org/10.1175/JAS-D-22-0207.1.

Qu, X., A. Hall, S. A. Klein, and P. M. Caldwell, 2014: On the spread of changes in marine low cloud cover in climate model simulations of the 21st century. *Climate Dynamics*, **42 (9-10)**, 2603–2626, https://doi.org/10.1007/s00382-013-1945-z.

Randall, D. A., 1980: Conditional instability of the first kind upside-down. *J. Atmos. Sci.*, **37 (1)**, 125–130, https://doi.org/10.1175/1520-0469(1980)037<0125:CIOTFK>2.0.CO;2.

Randall, D. A., J. A. Coakley Jr., D. H. Lenschow, C. W. Fairall, and R. A. Kropfli, 1984: Outlook for research on subtropical marine stratification clouds. *Bull. Amer. Meteor. Soc.*, **65**, 1290–1301.

Romps, D. M., 2008: The dry-entropy budget of a moist atmosphere. *J. Atmos. Sci.*, **65**, 3779–3799.

Salazar, A. M., and E. Tziperman, 2023: Exploring subtropical stratocumulus multiple equilibria using a mixed-layer model. *J. Climate*, 1–38, https://doi.org/10.1175/JCLI-D-22-0528.1.

Sandu, I., B. Stevens, and R. Pincus, 2010: On the transitions in marine boundary layer cloudiness. *Atmos. Chem. Phys.*, **10**, 2377–2391, https://doi.org/10.5194/acp-10-2377-2010.

Schalkwijk, J., H. J. J. Jonker, and A. P. Siebesma, 2013: Simple solutions to steady-state cumulus regimes in the convective boundary layer. *J. Atmos. Sci.*, **70 (11)**, 3656–3672, https://doi.org/10.1175/jas-d-12-0312.1.

Schneider, T., C. M. Kaul, and K. G. Pressel, 2019: Possible climate transitions from breakup of stratocumulus decks under greenhouse warming. *Nat. Geosci.*, **12 (3)**, 163–167, https://doi.org/10.1038/s41561-019-0310-1.

Scott, R. C., T. A. Myers, J. R. Norris, M. D. Zelinka, S. A. Klein, M. Sun, and D. R. Doelling, 2020: Observed sensitivity of low-cloud radiative effects to meteorological perturbations over the global oceans. *J. Climate*, **33 (18)**, 7717–7734, https://doi.org/10.1175/JCLI-D-19-1028.1.

Siebesma, A. P., and Coauthors, 2009: Cloud-controlling factors. *Clouds Perturbed Climate Syst. Their Relatsh. to Energy Balance Atmos. Dyn. Precip.*, MIT Press, 269–290.

Singer, C. E., and T. Schneider, 2023: CO_2-driven stratocumulus cloud breakup in a bulk boundary layer model. *J. Climate*, https://doi.org/tbd-b.

Stephens, G. L., 1978: Radiation profiles in extended water clouds. II: Parameterization schemes. *J. Atmos. Sci.*, **35 (11)**, 2123–2132, https://doi.org/10.1175/1520-0469(1978)035<2123:RPIEWC>2.0.CO;2.

Stevens, B., 2006: Bulk boundary-layer concepts for simplified models of tropical dynamics. *Theor. Comput. Fluid Dyn.*, **20 (5-6)**, 279–304, https://doi.org/10.1007/s00162-006-0032-z.

Stevens, B., and J.-l. Brenguier, 2009: Cloud-controlling factors: Low clouds. *Clouds Perturbed Climate Syst. Their Relatsh. to Energy Balance Atmos. Dyn. Precip.*, 1802, MIT Press.

Stevens, B., G. Vali, K. Comstock, R. Wood, M. C. van Zanten, P. H. Austin, C. S. Bretherton, and D. H. Lenschow, 2005: Pockets of open cells and drizzle in marine stratocumulus. *Bull. Amer. Meteor. Soc.*, 51–57, https://doi.org/10.1175/BAMS-86-1-51.

Tan, Z., T. Schneider, J. Teixeira, and K. G. Pressel, 2016: Large-eddy simulation of subtropical cloud-topped boundary layers: 1. A forcing framework with closed surface energy balance. *J. Adv. Model. Earth Syst.*, **8 (4)**, 1565–1585, https://doi.org/10.1002/2016MS000655.

Teixeira, J., and Coauthors, 2011: Tropical and subtropical cloud transitions in weather and climate prediction models: The GCSS/WGNE Pacific cross-section intercomparison (GPCI). *J. Climate*, **24 (20)**, 5223–5256, https://doi.org/10.1175/2011JCLI3672.1.

Uchida, J., C. S. Bretherton, and P. N. Blossey, 2010: The sensitivity of stratocumulus-capped mixed layers to cloud droplet concentration: Do LES and mixed-layer models agree? *Atmos. Chem. Phys.*, **10**, 4097–4109, https://doi.org/10.5194/acp-10-4097-2010.

Wood, R., 2012: Stratocumulus clouds. *Mon. Weather Rev.*, **140 (8)**, 2373–2423, https://doi.org/10.1175/MWR-D-11-00121.1.

Wood, R., and C. S. Bretherton, 2006: On the relationship between stratiform low cloud cover and lower-tropospheric stability. *J. Climate*, **19 (24)**, 6425–6432, https://doi.org/10.1175/JCLI3988.1.

Wyant, M. C., C. S. Bretherton, H. A. Rand, and D. E. Stevens, 1997: Numerical simulations and a conceptual model of the stratocumulus to trade cumulus transition. *J. Atmos. Sci.*, **54 (1)**, 168–192, https://doi.org/10.1175/1520-0469(1997)054<0168:NSAACM>2.0.CO;2.

Yamaguchi, T., G. Feingold, and J. Kazil, 2017: Stratocumulus to cumulus transition by drizzle. *J. Adv. Model. Earth Syst.*, **9 (6)**, 2333–2349, https://doi.org/10.1002/2017MS001104.

Zhang, Y., B. Stevens, B. Medeiros, and M. Ghil, 2009: Low-cloud fraction, lower-tropospheric stability, and large-scale divergence. *J. Climate*, **22 (18)**, 4827–4844, https://doi.org/10.1175/2009JCLI2891.1.

Zheng, Y., D. Rosenfeld, Y. Zhu, and Z. Li, 2019: Satellite-based estimation of cloud top radiative cooling rate for marine stratocumulus. *Geophys. Res. Lett.*, **46 (8)**, 4485–4494, https://doi.org/10.1029/2019GL082094.

Zheng, Y., Y. Zhu, D. Rosenfeld, and Z. Li, 2021: Climatology of cloud-top radiative cooling in marine shallow clouds. *Geophys. Res. Lett.*, **48 (19)**, e2021GL094 676, https://doi.org/10.1029/2021GL094676.